Sedimentary Geology 367 (2018) 135–145

Contents lists available at ScienceDirect

Sedimentary Geology

journal homepage: www.elsevier.com/locate/sedgeo

Visualisation and analysis of shear-deformation bands in unconsolidated Pleistocene sand using ground-penetrating radar: Implications for paleoseismological studies

Christian Brandes [a,*], Jan Igel [b], Markus Loewer [b], David C. Tanner [b], Jörg Lang [a], Katharina Müller [a], Jutta Winsemann [a]

[a] Institut für Geologie, Leibniz Universität Hannover, Callinstr. 30, 30167 Hannover, Germany
[b] Leibniz Institute for Applied Geophysics (LIAG), Stilleweg 2, 30655 Hannover, Germany

ARTICLE INFO

Article history:
Received 11 December 2017
Received in revised form 13 February 2018
Accepted 14 February 2018
Available online 16 February 2018

Editor: Dr. J. Knight

Keywords:
Deformation bands
Ground-penetrating radar
Neotectonics
Paleoseismology

ABSTRACT

Deformation bands in unconsolidated sediments are of great value for paleoseismological studies in sedimentary archives. Using ground-penetrating radar (GPR), we investigated an array of shear-deformation bands that developed in unconsolidated Pleistocene glacifluvial Gilbert-type delta sediments. A dense grid (spacing 0.6 m) of GPR profiles was measured on top of a 20 m-long outcrop that exposes shear-deformation bands. Features in the radargrams could be directly tied to the exposure. The shear-deformation bands are partly represented by inclined reflectors and partly by the offset of reflections at delta clinoforms. 3-D interpretation of the 2-D radar sections shows that the bands have near-planar geometries that can be traced throughout the entire sediment volume. Thin sections of sediment samples show that the analysed shear-deformation bands have a denser grain packing than the host sediment. Thus they have a lower porosity and smaller pore sizes and therefore, in the vadose zone, the deformation bands have a higher water content due to enhanced capillary forces. This, together with the partially-developed weak calcite cementation and the distinct offset along the bands, are likely the main reasons for the clear and unambiguous expression of the shear-deformation bands in the radar survey. The study shows that deformation-band arrays can clearly be detected using GPR and quickly mapped over larger sediment volumes. With the 3-D analysis, it is further possible to derive the orientation and geometry of the bands. This allows correlation of the bands with the regional fault trend. Studying deformation bands in unconsolidated sediments with GPR is therefore a powerful approach in paleoseismological studies. Based on our data, we postulate that the outcrop is part of a dextral strike-slip zone that was reactivated by glacial isostatic adjustment.

1. Introduction

Deformation bands are structural elements that develop in porous sandstones, tuffs and limestones and in unconsolidated granular material in the upper crust, in different tectonics settings and with various driving mechanisms, such as faulting and compaction (Fossen et al., 2007). In the former, for instance, they are likely to form during earthquakes (Cashman et al., 2007), and therefore can serve as important indicators for paleoseismic events. The characteristics of deformation bands are their relatively small offsets and their tabular geometry; thicknesses range from millimetres to centimetres (e.g., Aydin, 1978; Fossen et al., 2007). Three main types of deformation bands can occur. Du Bernard et al. (2002) showed dilation bands form due to pure extension (mode I) and compaction bands result from compaction (with pore space reduction). Shear-deformation bands show a distinct offset due to shear (mode II). A fourth type of deformation band is a so-called shear-enhanced compaction band that accommodates both shear and compaction (Eichhubl et al., 2010). Internally, shear-deformation bands may show a significant pore-space reduction compared to their host material, which results in their low hydraulic permeability (e.g., Hesthammer and Fossen, 2001; Shipton et al., 2005; Torabi and Fossen, 2009; Tindall, 2014). The pore-space loss has been suggested to be caused by compaction (Mollema and Antonellini, 1996) and/or cataclasis (Ballas et al., 2015).

Because their low permeability affects fluid flow in hydrocarbon reservoirs, deformation bands have attracted much attention over the last two decades. Consequently, deformation bands have been incorporated into reservoir simulations (Qu and Tveranger, 2016; Zuluaga et al., 2016). For this reason, it is important to understand their geometry and extent on a reservoir scale. Deformation bands can occur in different tectonic regimes (e.g., Ballas et al., 2015; Soliva et al., 2016) and

* Corresponding author at: Institute for Geology, Leibniz Universität Hannover, Callinstr. 30, 30167 Hannover, Germany.
E-mail address: brandes@geowi.uni-hannover.de (C. Brandes).

https://doi.org/10.1016/j.sedgeo.2018.02.005

are widely developed in fault-damage zones (e.g., Shipton and Cowie, 2001; Fossen et al., 2007). Understanding the formation and distribution of deformation bands is therefore important for different geoscience sub-disciplines, such as structural geology, petroleum geology, reservoir geomechanics and hydrogeology. The more recent observation that deformation bands also develop in unconsolidated near-surface sediments along active faults during earthquakes (Cashman et al., 2007) allows the use of deformation bands to indicate paleo-earthquakes and to help identify recently active faults. This makes the analysis of deformation bands highly relevant to the field of seismology, paleoseismology, neotectonics, and Quaternary geology.

However, deformation bands are below the resolution of most standard geophysical exploration methods, e.g., they are at the subseismic scale (Fossen et al., 2005; Ballas et al., 2015). Most outcrops only allow an analysis of deformation bands in 2-D, or in the case of unconsolidated material that can be sliced, limited 3-D analysis of volumes can be carried out. For instance, Brandes and Tanner (2012) analysed shear-deformation bands in three dimensions within a ca. 3 m^3 volume of unconsolidated sand. Their results show that some bands are slightly arcuate in strike direction, but the analysed volume was too small to generalise this. To analyse the geometry and orientation of deformation bands within a larger sediment volume (especially in strike direction), geophysical methods have to be used that are able to resolve these structures.

Geophysical methods are valuable to analyse near-surface faults (e.g., Bano et al., 2002). Due to its high resolution, ground-penetrating radar (GPR) has been widely used to obtain structural information in sedimentology (Bristow and Jol, 2003; Neal, 2004; Van Dam, 2012; Lang et al., 2017). It is also capable of mapping and characterising fractures in hard rock (e.g., Grégoire et al., 2003; Grasmueck et al., 2005; Theune et al., 2006; Dorn et al., 2012; Baek et al., 2017). It has been used to reveal detailed structural information of fault zones, including displacement estimates and off-fault deformation (Tronicke et al., 2006; McClymont et al., 2009; Christie et al., 2009). Medeiros et al. (2010) found evidence of deformation-band reflections in GPR data of a sandstone formation and used this as additional information for the hydraulic characterisation of the rock.

GPR investigation can be performed either in 2-D, i.e., single profiles are measured and interpreted, or in 3-D. Pseudo 3-D GPR means that measurements are carried out along a grid and individual profiles are processed and interpreted in 2-D, before a 3-D model is constructed using this information. This approach enables investigation of relatively large areas within a reasonable time scale and it is robust concerning surface topography. Full 3-D data (e.g., Grasmueck et al., 2005; Van Dam, 2012) requires very dense spatial sampling (less than a quarter wavelength) in both inline and crossline directions, thus this is time consuming and requires near-flat surfaces. Full 3-D GPR provides very high-resolution images of the subsurface, even in complex 3-D settings, such as, e.g., fracture networks, independent of the orientation of the measuring campaign.

In this study, we analyse the 3-D geometry of an array of shear-deformation bands that developed in Middle Pleistocene unconsolidated deltaic sands in northern Germany using pseudo 3-D GPR. We show that this approach is an effective and efficient way to visualize and analyse the deformation bands through large sediment volumes. GPR is able to close the gap between a 2-D outcrop analysis and the 3-D approach of industrial 3-D reflection seismics, which is usually unable to resolve structures at the scale of deformation bands (e.g., Chwatal et al., 2015; Ercoli et al., 2015; Lang et al., 2017).

2. Geological setting

The study area is located in NW Germany, 24 km SSW of Hildesheim (Fig. 1), and belongs to the Central European Basin System (CEBS). The CEBS evolved on top of a Carboniferous Variscan foreland basin (Betz et al., 1987). During the early Permian, an E-W directed, extensional tectonic phase affected the area (Lohr et al., 2007), and a wide continental rift basin was formed (van Wees et al., 2000), which is characterized by N-S striking graben structures (Gast and Gundlach, 2006). Ongoing fault activity and subsidence occurred throughout the Mesozoic (van Wees

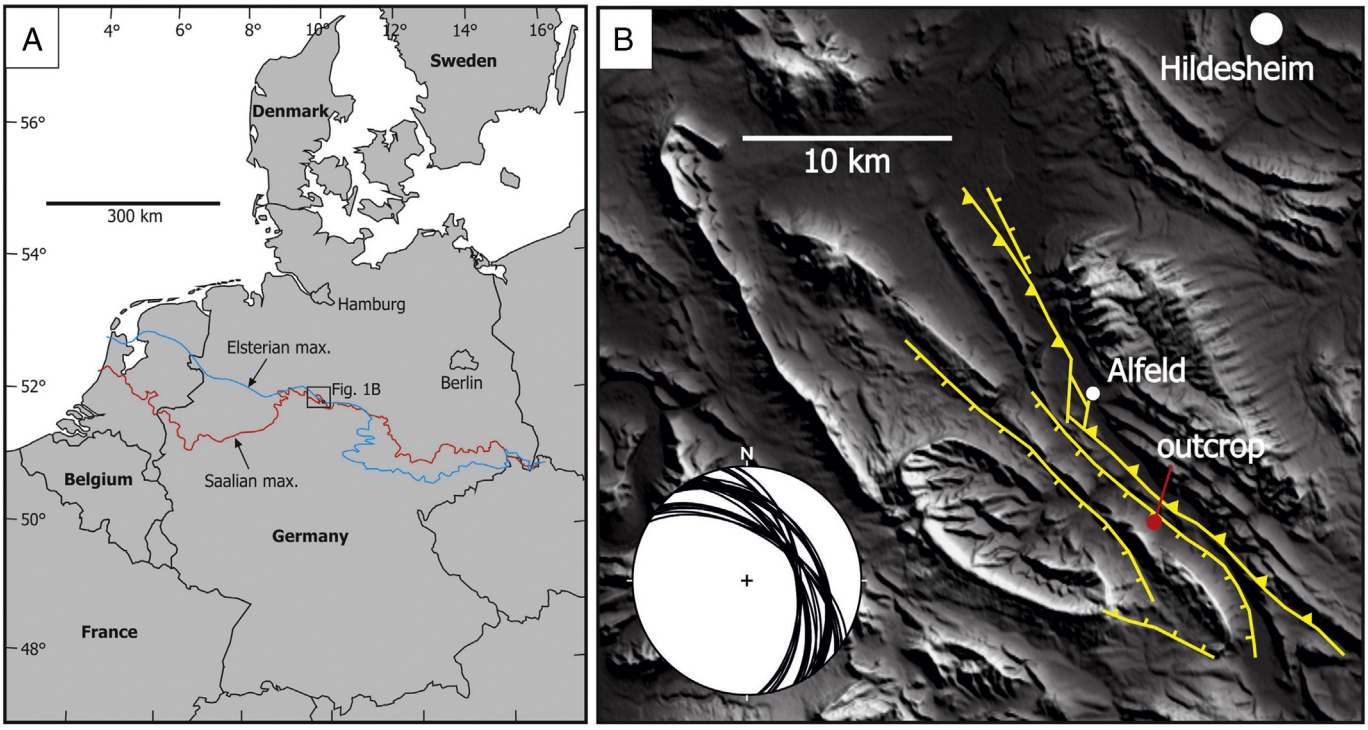

Fig. 1. Location map and geological setting. (A) Location of the study area in northern Germany. Extent of the Elsterian and Saalian glaciation after Roskosch et al. (2015). (B) Digital elevation model of the study area, illustrating the large fold structures and the fault pattern. Stereographic projection showing the trend of the shear-deformation bands measured in the outcrop. These bands have the same trend as the major Mesozoic faults. The DEM is based on SRTM data; the fault pattern is from Baldschuhn et al. (1996).

et al., 2000; Lohr et al., 2007). During this phase, possibly related to a Jurassic transtensional phase (Lohr et al., 2007), the major basement faults shown in Fig. 1B probably formed.

This was followed by a NNE-SSW directed contractional phase (Kley et al., 2008; Brandes et al., 2013; Tanner and Krawczyk, 2017) that led to inversion of the basin-fill during the late Cretaceous (Baldschuhn et al., 1991; Kockel, 2003; Kley and Voigt, 2008). The large-scale fold structures in Fig. 1B formed during this event.

During the Middle Pleistocene glaciations, the study area was repeatedly covered by proglacial lakes, which formed in front of the Elsterian and Saalian Scandinavian ice sheets during Marine Isotope Stages (MIS) 12 to 6 (Winsemann et al., 2007; Roskosch et al., 2015; Lang et al., 2018). At the study site, along the northern margin of glacial Lake Leine, an ice-marginal delta complex formed, which is up to 60 m thick and has a length of 1.5 km and a width of approximately 1 km (Winsemann et al., 2007; Lang et al., 2017). Based on depositional architecture and luminescence dating, two genetically different delta bodies can be distinguished that probably formed during two transgressive-regressive cycles during MIS 8 and 6 (Roskosch et al., 2015). The older sand-rich Gilbert-type delta deposits (MIS 8) were probably shed from the northeast via a bedrock feeder channel (Winsemann et al., 2007). Within these delta deposits, numerous shear-deformation bands are developed (Brandes and Tanner, 2012). During the second ice advance (MIS 6), an ice-contact delta formed in front of an ice lobe that terminated in the lake. These delta deposits were shed from northwesterly directions, contain flow-till layers and some minor glaciotectonic thrusts, and unconformably overlie or downlap the older delta system (Winsemann et al., 2007; Roskosch et al., 2015).

3. Database and methods

3.1. Acquisition and processing of the ground-penetrating radar data

We used a SIR-4000 GPR system with 200 MHz shielded antennas for data acquisition. Position and elevation of the GPR antenna was logged using a Trimble 5800 differential global positioning system (DGPS) with centimetre accuracy to determine the lateral position and elevation. Survey lines were measured on top of a 20 m long outcrop, on a regular grid of 10 m × 14 m with 0.6 m line spacing (Fig. 2), resulting in a pseudo 3-D dataset of the volume. GPR data were sampled with a trace distance of 3 cm in the inline direction, triggered by an odometer. The deviation of the GPR tracks from straight lines was caused by the microtopography of the ground surface. The GPR antenna was pulled by a rope that is not able to control drift perpendicular to the measuring direction, which depends on the slope of the ground surface. As the GPS antenna is mounted on a pole above the centre of the GPR antenna, tilting of the GPR antenna leads to an apparent moderate offset of the position.

Data processing comprised time-zero correction, amplitude balancing by compensating spherical divergence and exponential attenuation (4 dB/m), dewowing (5 ns time window) and bandpass filtering (cos taper with 30/60 MHz for the lower cut/plateau frequency and 350/500 MHz for the upper plateau/cut frequency). The data were finally depth migrated and topographically corrected so that the reflectors appear at the correct position and show the correct dips. We assessed radar-wave velocity by analysing the curvature of a diffraction hyperbola of an iron rod as an artificial diffractor and by varying the velocity for topographic correction until the groundwater table reflection appeared horizontal. We used a constant radar-wave velocity of 0.12 m ns^{-1}, which is a typical value for the vadose zone in sand (Igel et al., 2013). Diffraction hyperbolas were observed in the original data at positions where reflectors ended at deformation bands and were effectively focused by the migration process. The low-loss sandy material at the site enabled investigation depths of up to 6 m with the 200 MHz antenna.

3.2. Building a 3-D geological model

We derived a 3-D model by placing the GPR sections (001–016; Fig. 2) in their correct geographical location and orientation into the software package Move™. Individual shear-deformation bands were first interpreted on the 2-D sections. The sections close to the outcrop were

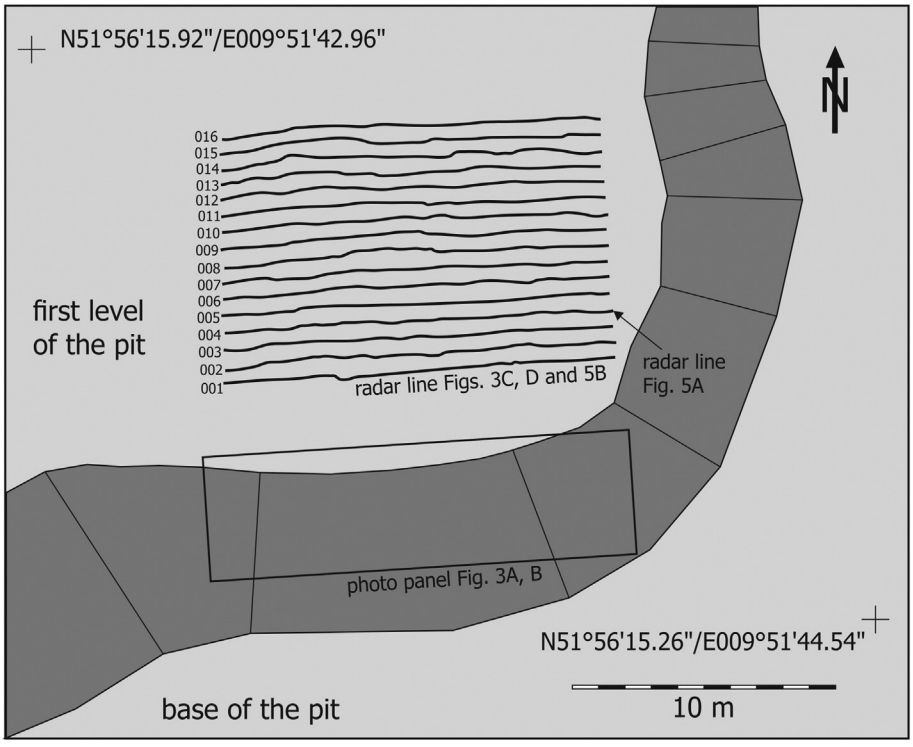

Fig. 2. Map of the GPR survey lines according to DGPS tracking. The E-W trending lines trend perpendicular to the strike of the shear-deformation bands. Lines 001–016 are 14 m long and have a spacing of approximately 0.6 m. They were measured using a 200 MHz antenna.

used to assign the reflectors to bedding planes and deformation bands. Then the main structures were subsequently tracked on the other 2-D sections up to line 16, which is approx. 11 m north of the outcrop (Fig. 2).

2-D fault traces were picked on the radargrams. These data were interpolated using a cubic Bézier spline algorithm to form irregularly triangulated 3-D mesh surfaces. Each surface consisted of ca. 300 triangular elements. Attributes of the triangles were then determined (dip, strike azimuth). Curvature of the surface was determined by comparing a triangular element with its neighbouring elements. This was then attributed to the middle element.

Stereographic projections were then made of the triangular elements that make up the deformation-band surfaces (each element is represented as a plane that is displayed as a great circle on the stereographic projection).

4. Results

4.1. Outcrop data

We classify the observed structures as shear-deformation bands because they offset bedding. They can be distinguished from shear-enhanced compaction bands because of their higher dip angle, with a maximum dip of 58°. They are mainly developed within foreset deposits of the older Gilbert-type delta complex. These foreset deposits consist of steeply-dipping, medium- to very thick-bedded sand and pebbly sand. Coarser-grained pebbly sand and sand beds commonly comprise backset cross-stratification and low-angle cross-stratification (Fig. 3), deposited by supercritical turbidity currents. The coarse-grained, foreset-bed packages laterally pass into finer-grained foreset-bed

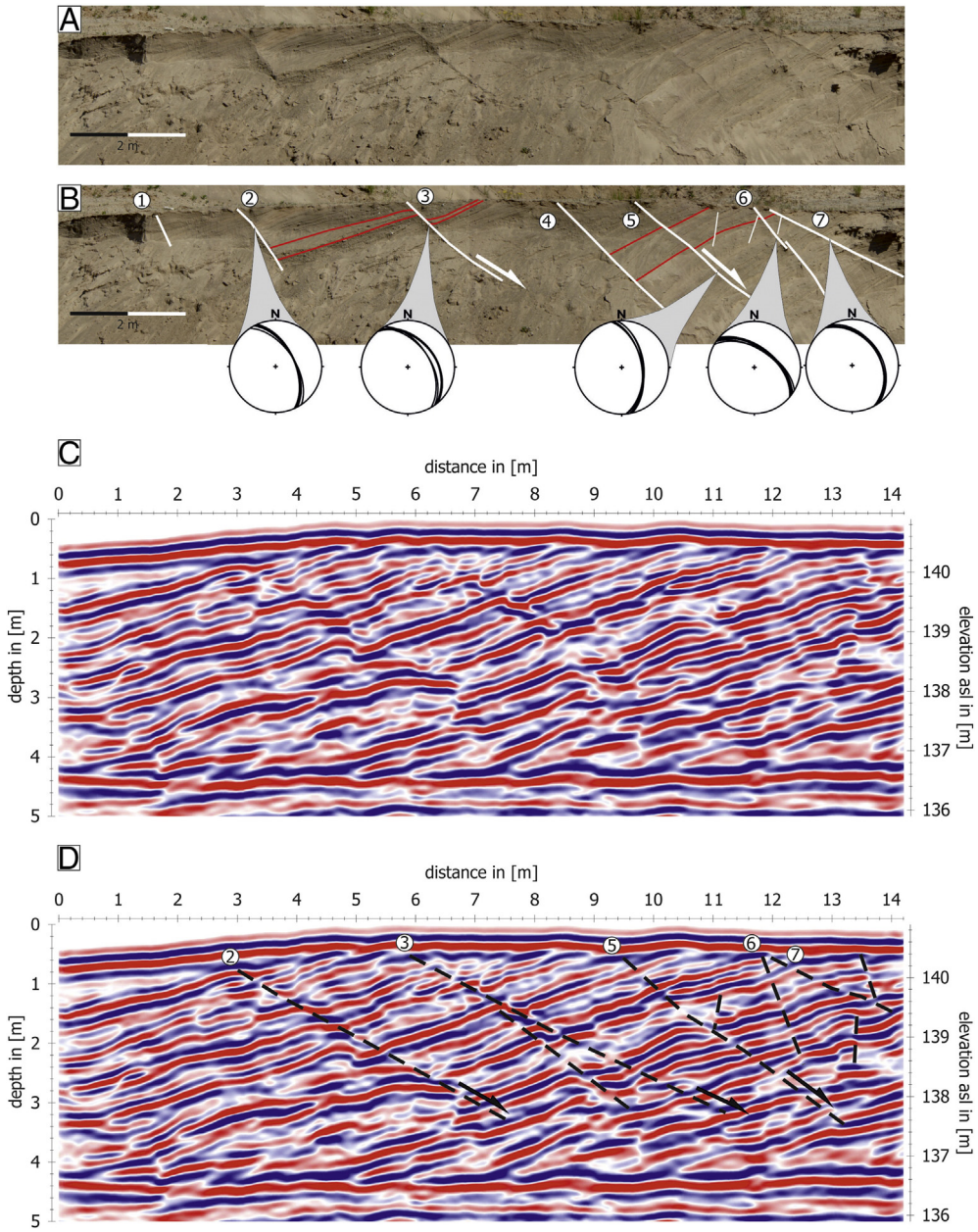

Fig. 3. Outcrop data. (A) Outcrop face that exposes seven major, north-eastward dipping shear-deformation bands in delta foreset deposits with backset cross-stratification. (B) Interpretation of the outcrop. The shear-deformation bands have dip angles of 36–58°. Between shear-deformation bands 5 and 7, three shorter antithetic bands are developed with higher dip angles. (C) Processed GPR line 001, (with automatic gain control, AGC). (D) Interpretation of line 001. Five of the seven shear-deformation bands that are exposed at the outcrop surface can be identified by the offset of reflectors, which represent delta clinoforms. The bands are partly expressed as discontinuous reflectors and partly as zones with low amplitude.

packages with dune-scale cross-stratification and climbing-ripple cross-lamination, indicating less powerful subcritical turbidity currents (Winsemann et al., 2007; Lang et al., 2017). The foreset-bed packages are unconformably overlain by a younger, coarse-grained, incised-valley fill that is MIS 6 in age and crosscuts the shear-deformation bands, thus implying the shear-deformation bands only belong to the older complex.

The shear-deformation bands exposed in the analysed 2-D outcrop have a normal sense of displacement in a range of centimetres to decimetres, and form a uniform, northeastwardly-dipping, array. Altogether seven major bands developed with a spacing of 1 to 2 m. Individual bands dip eastward between 30° and 58° (Fig. 3A). The offset of the shear-deformation bands is in the range of 1 to 24 cm (the highest is in band 3). Thicknesses of the bands vary between 1 and 3 cm (the highest is in band 3). At one location on the analysed section, between shear-deformation bands 5 and 6, two shorter antithetic bands are developed that have higher dip angles. The presence of the antithetic bands is very common in deformation bands, since they back up the normal offsets. These bands have lower offsets of 1 cm and a thickness of 0.5 cm. All seven major bands in the 2-D outcrop have overall straight traces in the dip direction (Fig. 3B). Some of the bands show a weak calcite cementation (Fig. 4). Brandes and Tanner (2012) described that there were at least two stages of calcite overgrowth in deformation bands from this site.

Thin-section analysis of band 7 shows that the grains have much denser packing within the deformation bands, with respect to the host sediment (Fig. 4). All the grains are rounded to subrounded (according to the scheme of Pettijohn et al., 1973). There is no change in grain morphology or size from the host sediment to the shear deformation band (Fig. 4), i.e., we see no evidence of cataclasis within the deformation band. This was also the conclusion of Brandes and Tanner (2012). We infer grain-boundary sliding and reorientation as the deformation mechanism.

4.2. Ground-penetrating radar data

The E-W trending GPR surveys, parallel to the outcrop face, are oriented near perpendicular (up to 30° deviation) to the strike of the deformation bands (Fig. 3). The reflections that are inclined to the west represent delta clinoforms. The groundwater table causes the strong horizontal reflection at approximately 4 m depth. The migrated GPR profiles clearly show five of the seven deformation bands that are exposed in the outcrop (Fig. 3). The bands can be identified by the systematic offset of reflectors, which represent the sedimentary bedding (Fig. 3C, D). Partly the bands are expressed as inclined reflections that interfere with reflections from sedimentary bedding. Partly they are expressed as transparent zones with near-zero amplitude along inclined lines where a phase shift of bedding reflectors appears. The deformation bands could also be identified in the unmigrated sections (not shown here); they are represented by diffraction hyperbolas at the truncations of the sedimentary reflectors at the deformation bands. In the section in Fig. 5A, the shear-deformation bands can also be identified by reflector offsets, as well as by distinct reflectors that can be traced down to 4 m below the topographic surface.

On the 2-D GPR profiles the bands have an overall straight-line geometry, but some bands also show slight bends (Fig. 3D). The dip angle of the shear-deformation band reflectors matches the dip angles measured in the outcrop (Fig. 3B). At shear-deformation band 2, the GPR (Line 001) shows a systematic offset decrease towards the topographic surface (Fig. 5B). This indicates upward propagation of the deformation band. At the tip of the band a monocline is developed that we interpret as an extensional fault-propagation fold (Fig. 5B).

4.3. Geometry of the shear-deformation bands in 3D

Based on the interpretation of the pseudo 3-D radar data we constructed the deformation-band geometries in 3-D. The shear-deformation bands can be traced throughout the entire imaged volume, from the outcrop to the line 016 (Figs. 2, 3, 6A, B).

Shear-deformation band 2 has a planar geometry and is straight along-strike (Fig. 6B). The curvature is very low (Fig. 6C). Bands 3 and 5 also have a planar geometry. The curvature is restricted to a narrow zone, where slight along-strike bends are developed in these shear-deformation bands. From the 3-D model it became evident that bands 3 and 5 merge into a single band northwards. Shear-deformation band 6 is planar, but is slightly bent along-strike. Band 7 has a more curved geometry (Fig. 6C). The strong bend in the northern part of this shear-deformation band could either be an abrupt change in the along-strike geometry of the band or branching similar to the situation at shear-deformation band 3/5. Short antithetic deformation bands are also developed in the outcrop (Fig. 3A, B) and one of them is very pronounced on the radar surveys (Fig. 6B). It has a planar geometry with a strong bend developed at the northern end.

Stereographic projections of all the deformation-band surfaces in the 3-D model show the orientation of the major north-eastward-dipping shear-deformation bands (Fig. 6D, left). Their strike and dip closely matches the orientation of the bands measured with a Freiberg compass in the outcrop (Fig. 6D, right).

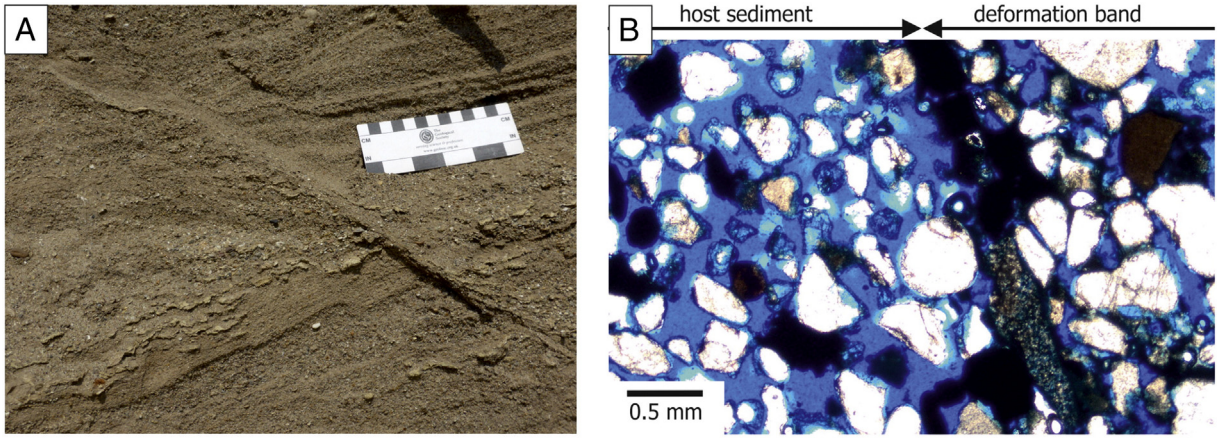

Fig. 4. (A) Photograph of shear-deformation band 7. The band has a thickness of 2–3 cm. (B) Thin-section of shear-deformation band 7. Blue resin was used in the thin section preparation to visualize the pore space. Calcite is precipitated within and along the edge of the deformation band. The pore space is higher in the host sediment (ca. 35%) than in the band (ca. 13%).

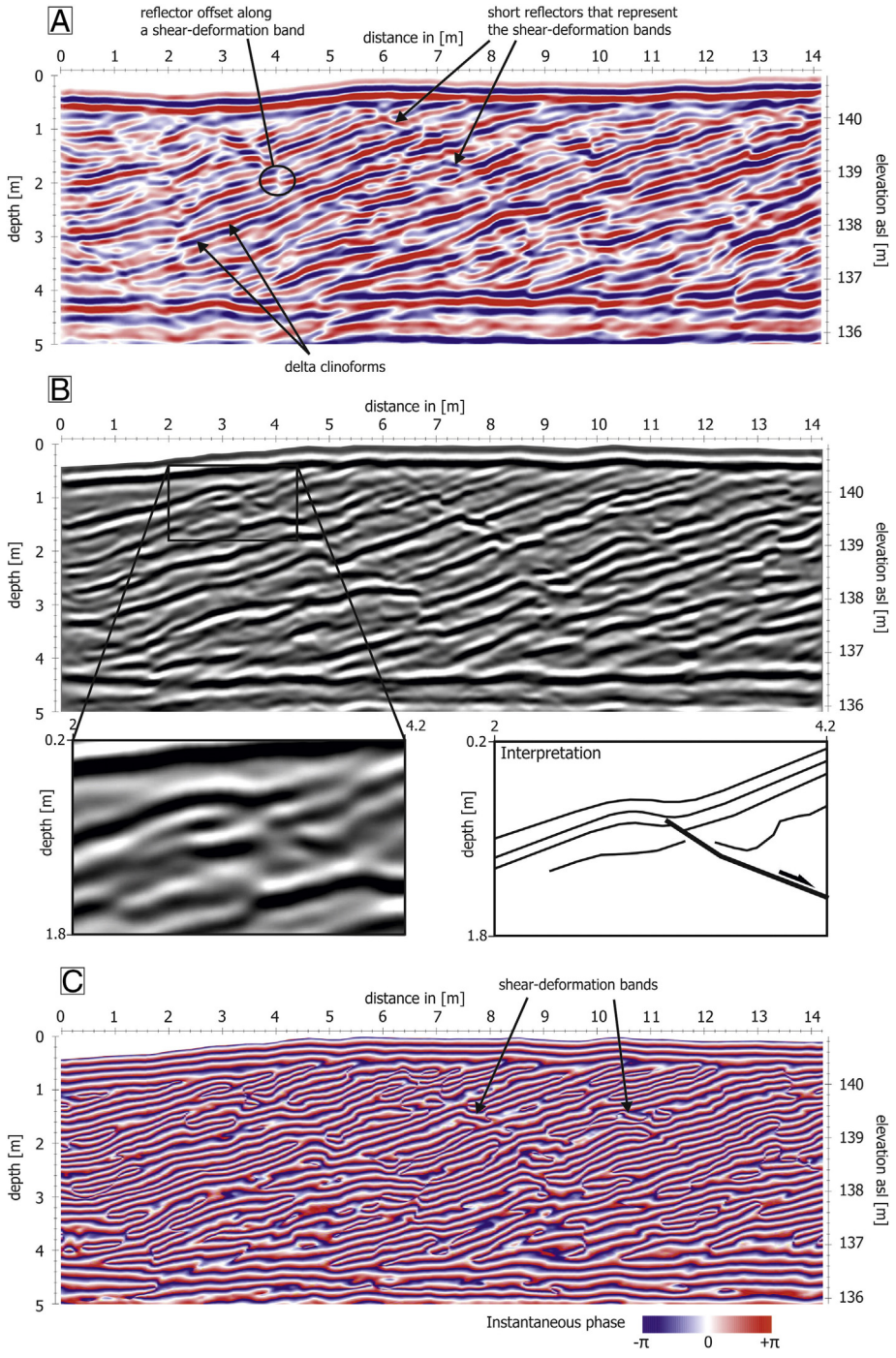

Fig. 5. (A) Processed GPR line 004 (amplitudes with AGC). The shear-deformation bands are partly represented by inclined reflectors and partly by the offset of reflectors. (B) The greyscale display allows to visualize offset variations along the shear-deformation band. At the tip of one of the bands, an extensional fault-propagation fold is developed. (C) Instantaneous phase of processed radar section highlighting displacements at deformation bands.

5. Discussion

5.1. The ability of GPR to visualise deformation bands

Various studies have shown that GPR can be used to investigate near-surface faults (e.g., Busby and Merritt, 1999; Liner and Liner, 1997; Demanet et al., 2001; Carpentier et al., 2012; Beauprêtre et al., 2012; Kettermann et al., 2015; Drahor and Berge, 2017) and fractures (Stevens et al., 1995; Baek et al., 2017). However, in many cases, the faults were detected only on the basis of reflector terminations (Meschede et al., 1997), which is often the only indication for steeply-dipping fault surfaces, and isolated 2-D surveys often fail to image faults due to out-of-plane reflections (McClymont et al., 2008b). Interpreting GPR images of fault zones is often difficult due to the structural complexity of the setting, the limited size of the fault-related microfacies and due to variations in the dielectric properties that are not necessarily connected with faulting (Salvi et al., 2003). Medeiros et al. (2010) for instance visualised deformation bands in sandstone using GPR. They showed that the bands are expressed on the radar surveys as low amplitude stripes. However, difficulties remained to detect the bands because of the small offsets on the individual bands and the fact that they have the same lithology as the host material. As for seismic image analysis,

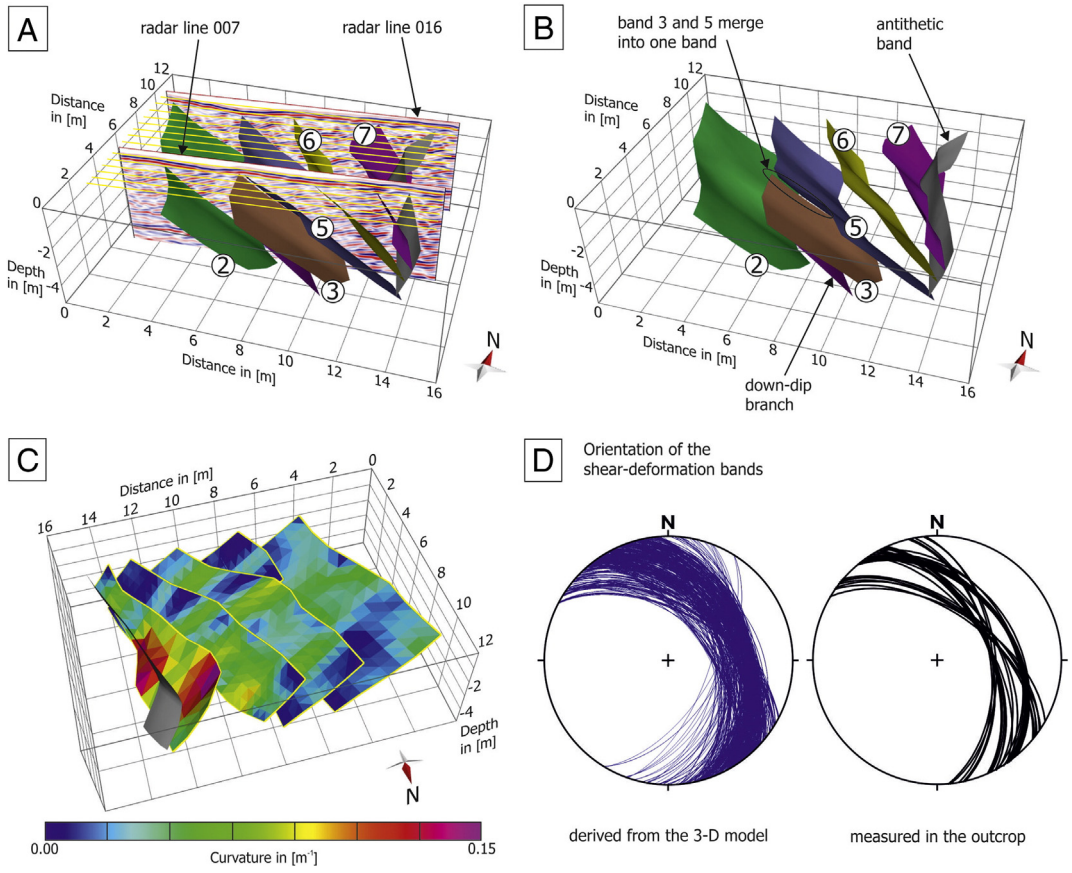

Fig. 6. 3-D geometrical modelling. (A) Perspective view of the 3-D model. Yellow lines represent GPR profiles (see Fig. 2); radar lines 007 and 016 are displayed. (B) Shear-deformation band 3 and 5 merge northward to a single band. (C) 3-D model with surfaces coloured by curvature, showing that the deformation bands are mostly planar or concave to the east and upwards. The local higher curvature of band 6 and 7 is caused by along-strike bends developed along these bands. (D) Stereographic projection of the shear-deformation band surfaces derived from the 3-D GPR model (blue great circles) compared to the orientation of the bands measured in the outcrop (black great circles).

GPR data interpretation of faults and other structures can be supported by attribute analysis (e.g., Grasmueck et al., 2005; McClymont et al., 2008a, 2008b; Forte et al., 2012), especially if full 3-D high quality data are available. However, most of the shear-deformation bands in our study can be clearly detected in the GPR images, in part expressed as distinct reflectors (Fig. 5). In addition, we calculated the instantaneous phase attribute, which was able to highlight the offset of the deformation bands (Fig. 5C). In this location, the dip of 30–60°, which is characteristic for normal faulting, may have favoured distinct GPR reflections from the bands, while significantly steeper planes might have been more challenging to map and would therefore need further analysis techniques. GPR also benefits from the low attenuation of the sandy material at this location, which enables the used antenna to investigate to a large depth.

The lower porosity of the bands with respect to the host material and the partly-developed weak calcite cementation of the shear-deformation bands are likely the main reasons for the distinct reflections produced by the bands. Firstly, the decrease of porosity has a direct influence on dielectric permittivity of the bulk material. Contrasts in permittivity cause reflections of electromagnetic waves. A secondary effect might be a stronger capillary force within the denser shear-deformation band, and therefore the higher water content of the shear-deformation band compared to the host material. We suggest that the contrast in water content, that causes a strong contrast in dielectric permittivity, is the main cause of GPR reflections at sedimentary bounding surfaces (Van Dam and Schlager, 2000), and probably it is also the main cause of the reflections of the deformation bands in this work.

It is important to note the special character of these shear-deformation bands in comparison to other deformation bands. In contrast to compaction bands and dilation bands, shear-deformation bands are characterised by a distinct offset (Du Bernard et al., 2002; Aydin et al., 2006). In outcrop, the offsets along the shear-deformation bands are in a range of centimetres to several decimetres (Fig. 3A). Some of the low-offset shear-deformation bands are clearly single bands, whereas the high-offset shear-deformation bands may be clusters, but this is difficult to decipher in this outcrop, in which the bands have also been altered by fluid flow and calcite precipitation.

These offsets can be clearly identified in the radargrams by following reflections at bedding planes, which are inclined to the west and represent delta clinoforms (Lang et al., 2017) (Fig. 3C, D). The offset of the sediments also juxtaposed different sediment facies, which might enhance the dielectric permittivity contrast across the shear-deformation band and thus cause reflections of the electromagnetic waves.

5.2. 3-D geometry of the shear-deformation bands

Brandes and Tanner (2012) showed that the 3-D geometry of deformation bands in unconsolidated sediments in a sediment volume of 3.38 m^3 could be studied, because the sediments can be sliced by hand. But this was nevertheless a very limited volume and slicing larger sediment volumes would be very time consuming and difficult due to the low stability of the material.

This study shows that GPR offers the opportunity to trace shear-deformation bands across much larger sediment volumes. The results indicate that the analysed shear-deformation bands have a planar and straight geometry over 9 m along-strike. Deformation bands typically branch and merge (Fossen et al., 2007) and individual bands are often hard linked (Fossen and Hesthammer, 1997). The Freden sand pit

exposes several shear-deformation bands that exhibit branching, where the bands split down dip. Along-strike branching is more difficult to detect in a vertical 2-D outcrops, such as present in the analysed sand pit. Therefore, 3-D analysis of GPR data offers the possibility to access hidden deformation band branching in a non-destructive and fast manner. The GPR data shows that band 3 has a down-dip branch and laterally merges with band 5 to a single band. The main shear-deformation band and its branch have planar geometries and are both planar along-strike (Fig. 6).

The smaller antithetic deformation bands are not very pronounced in the outcrop. These bands are thinner and less cemented compared to the major northeastward-dipping bands. They are also shorter in the dip direction (Fig. 3A). In contrast, on the radar lines one of the antithetic deformation bands can be clearly detected and mapped across several sections (Fig. 6A, B).

At the tip of shear-deformation band 2, a structure is developed that we interpret as an extensional fault-propagation fault (Fig. 5B). Similar structures develop in extensional regimes on different scales (Sharp et al., 2000; Khalil and McClay, 2002) and have been reproduced by modelling approaches (Hardy and McClay, 1999; Jin and Groshong, 2006).

5.3. Implications for paleoseismology

This work shows that deformation-band arrays can be easily detected with GPR and quickly mapped over larger sediment volumes. A 3-D model of the deformation bands allows to derive their orientations. GPR has been used to analyse active faults in different settings (Cai et al., 1996; Chow et al., 2001; Green et al., 2003; Reiss et al., 2003; Grützner et al., 2012, 2016). McClymont et al. (2008a, 2008b), and Christie et al. (2009) have shown that GPR has also the potential to detect small off-fault deformation structures that are commonly not resolved by digital elevation models, aerial photographs, or surface observations.

Clearly, deformation bands could have a glaciotectonic origin (Fossen et al., 2007). We cannot completely rule out glaciotectonic deformation (deformation in near-surface sediments, directly caused by an advancing glacier, by telescoping, shearing or loading of the sediments) as a driver for the origin of the shear-deformation bands. However, many of the deformation bands exposed in the sand pit follow the trend of the regional fault pattern (Fig. 7), indicating a close connection between the pre-existing Mesozoic faults and the Pleistocene deformation bands (Figs. 1, 7). The deformation bands might therefore reflect fault propagation and the related deformation above the tip of the reactivated basement faults. An alternative explanation for the coincidence between the orientation of the deformation bands and the basement faults would be differential compaction across buried fault scarps.

In addition, the deformation bands in the sand pit can be grouped into two sets. One NW-SE striking set follows the trend of the regional basement-fault pattern (Baldschuhn et al., 1996) (Fig. 1B), and one set strikes roughly perpendicular to this trend, forming a S-shape pattern. This geometry would fit a model of a strike-slip fault system (Figs. 7, 8). The recent stress field in this area has a roughly N-S oriented horizontal σ_{Hmax} (Reicherter et al., 2005) and would allow right-lateral movement along this strike-slip system. Therefore, we assume that right-lateral strike-slip movements occurred along the NW-SE trending basement faults under this stress field (Fig. 8). Between the basement faults, a NNE-SSW striking subordinate pull-apart structure evolved, which controlled the sediment distribution in the area and the orientation of the deformation bands (Fig. 8). In summary, these observations support the interpretation that the exposed shear-deformation bands are more likely the result of neotectonic movement, rather than glacial tectonics.

Deformation bands are often formed in the so-called 'process zone' ahead of the fault tip (Fossen et al., 2007). Cashman et al. (2007) and Shipton et al. (2017) have shown that deformation bands can be important indicators of co-seismic slip. This combination makes deformation bands very powerful for paleoseismological studies. Their occurrence can indicate faults in the subsurface and allows the identification of past seismic events, which is a major step towards seismic hazard analysis of a region. Especially in areas like northern Germany, where fault scarps are seldom developed because they were rapidly destroyed due to the climatic conditions (Kaiser, 2005), deformation bands are valuable hints to neotectonic movement. In Middle Jurassic times, northern Germany was affected by an E-W directed transtensional tectonic phase that created NW-SE oriented strike-slip- and normal faults (Lohr et al., 2007). We assume that the NW-SE trending basement faults in the study area also first evolved during this period (Fig. 1B). As discussed above, the shear-deformation bands analysed in this study most likely formed above the tip line of these presently-buried Mesozoic faults. This is supported by observation of shear-deformation band 2, where the GPR data shows a systematic offset decrease towards the topographic surface, where an extensional fault-propagation fold is developed (Fig. 5B), which indicates upward propagation of the deformation band. However, a single observation does not mean that all the deformation sets developed in this way.

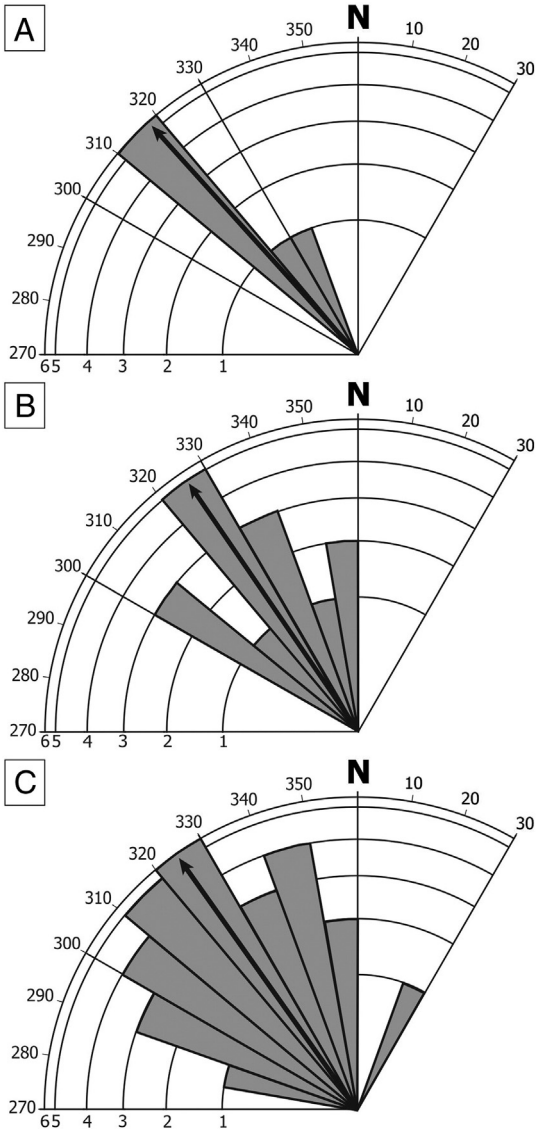

Fig. 7. Rose diagrams to illustrate the distribution of the strike of (A) the basement faults, shown in Fig. 1, (B) the deformation bands exposed in the outcrop (see Fig. 3A, B), and (C) the splined surfaces of the deformation bands in the 3-D model (see Fig. 6). Bold arrows represent the mean strike directions.

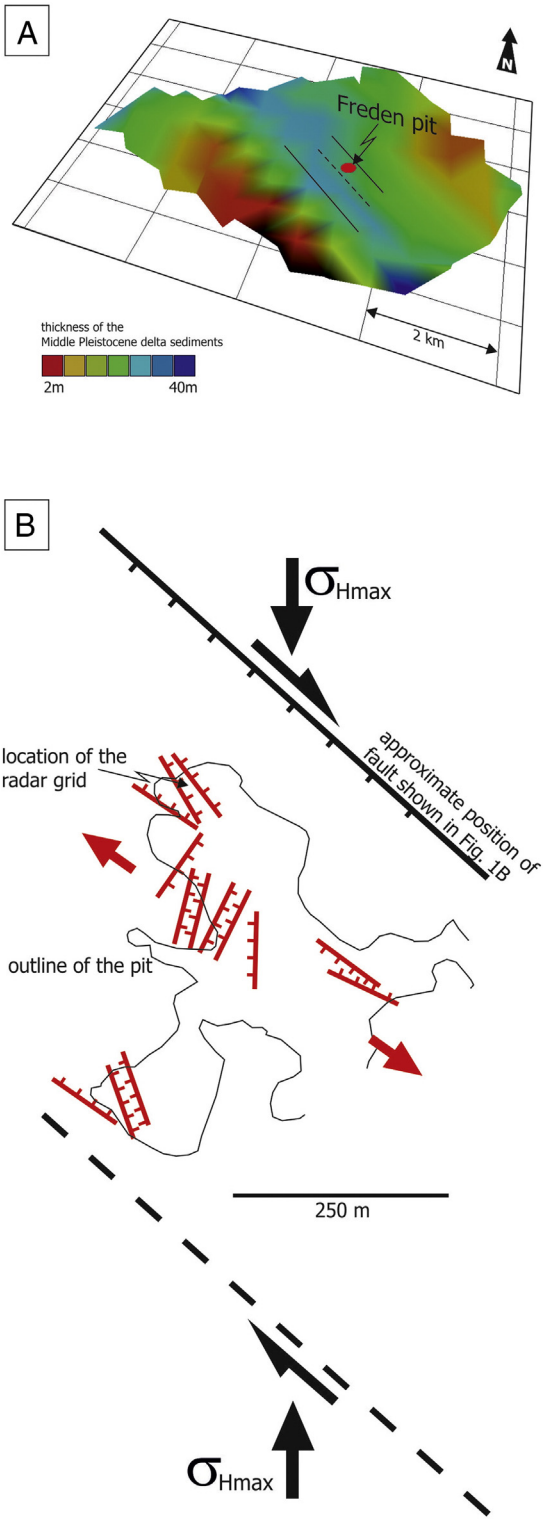

Fig. 8. (A) Sediment thickness map of the Freden delta complex, based on published borehole data from the LBEG data repository (https://www.lbeg.niedersachsen.de/kartenserver/nibis-kartenserver-72321.html). The highest sediment thickness occurs between the major basement faults, shown in B). (B) Map of the sand pit showing the representative strike directions of the deformation band sets and the regional basement faults. Dextral transtensive strike-slip on the basement faults with internal extension would best explain this strike pattern.

We suggest that the young tectonic activity along the Mesozoic basement faults was most likely reactivation due to lithospheric stress changes caused by glacial isostatic adjustment during the Middle Pleistocene (MIS 8). This is the most logical conclusion, based on the timing of faulting and the geometrical relationship to basement structures. Similar observations were made by Brandes et al. (2011) for the Middle Pleistocene Emme delta. Brandes et al. (2012) and Brandes and Winsemann (2013) also showed neotectonic activity along the Osning Thrust in northern Germany, which was reactivated after the Late Pleistocene Weichselian (MIS 2) glaciation. The shear-deformation bands exposed in the outcrop may have formed as co-seismic features and thus are potential indicators for paleo-earthquakes. However, we cannot rule out that the shear-deformation bands exposed in the study area formed during aseismic slip. The study demonstrates that GPR is ideally suited to map shear-deformation bands in unconsolidated sediments in 3-D. Therefore, it is also applicable for paleoseismological studies.

6. Conclusions

Deformation bands can serve as indicators of paleo-earthquakes and thus are important structural elements that can help to better estimate the seismic hazard potential of a region. With GPR it is possible to analyse the deformation bands in unconsolidated sediments along potential seismogenic faults. The results of this study can be summarised as:

1. GPR surveying is a non-destructive and quick method to map 3-D deformation-band geometry in a large sediment volume.
2. Shear-deformation bands developed in unconsolidated sediments can be clearly detected with GPR. They are expressed on the radar surveys by both reflector offsets and distinct reflections from the deformation bands themselves.
3. The orientation of the shear-deformation bands based on structural measurements with a compass in the outcrop in comparison with the orientation of the bands derived from the 3-D model shows that GPR data can be used to derive a reliable image of the structures behind the outcrop.
4. The 3-D analysis shows that the shear-deformation bands in this study follow the trend of the regional fault pattern. This indicates a direct relationship of the deformation bands to potential deep-seated faults. We therefore conclude that the analysed shear-deformation bands formed as near-surface expression of fault movement at depth.
5. It is important to consider deformation-band geometry, not only in hydrocarbon-related reservoir simulations, but also in exploration for groundwater, since they often show different hydraulic properties to that of the host material.
6. Interestingly, most of the deformation bands caused clear GPR reflections, although some were only visible on the basis of terminations and displacements of reflections at bedding planes, albeit with a similar dip. This could be caused by differences in slip, or differences in pore-size distribution and water content and thus the dielectric contrast in the deformation bands. Future work will concentrate on investigating the causes of the reflection and the differences between the bands.

Acknowledgements

We would like to thank the owner of the Ulrich sand pit in Freden for the permission to enter his property and to carry out geological work. D. Epping and R. Meyer (LIAG) assisted the GPR surveying. Partial funding of the research work by Leibniz Forschungsinitiative FI:GEO (Leibniz Universität Hannover) is greatly appreciated. Midland Valley Exploration Ltd. is gratefully thanked for an academic license for Move™. We thank H. Fossen, J. Knight, Z. Shipton and R. Van Dam for detailed and highly constructive reviews.

References

Aydin, A., 1978. Small faults formed as deformation bands in sandstone. Pure and Applied Geophysics 116, 913–930.

Aydin, A., Borja, R.I., Eichhubl, P., 2006. Geological and mathematical framework for failure modes in granular rock. Journal of Structural Geology 28, 83–98.

Baek, S.-H., Kima, S.-S., Kwon, J.-S., Um, E.S., 2017. Ground penetrating radar for fracture mapping in underground hazardous waste disposal sites: a case study from an underground research tunnel, South Korea. Journal of Applied Geophysics 141, 24–33.

Baldschuhn, R., Best, G., Kockel, F., 1991. Inversion tectonics in the north-west German basin. In: Spencer, A.M. (Ed.), Generation, Accumulation and Production of Europe's Hydrocarbons. Special Publication of the European Association of Petroleum Geoscientists vol. 1. Oxford University Press, Oxford, pp. 149–159.

Baldschuhn, R., Binot, F., Fleig, S., Kockel, F., 1996. Geotektonischer Atlas von Nordwest-Deutschland und dem deutschen Nordsee-Sektor. Geologisches Jahrbuch Reihe A 153. Schweizerbart, Stuttgart (88 pp.).

Ballas, G., Fossen, H., Soliva, R., 2015. Factors controlling permeability of cataclastic deformation bands and faults in porous sandstone reservoirs. Journal of Structural Geology 76, 1–21.

Bano, M., Edel, J.B., Herquel, G., 2002. EPGS Class 2001–2002. Geophysical Investigation of a Recent Shallow Fault 21. The Leading Edge, pp. 648–650.

Beauprêtre, S., Garambois, S., Manighetti, I., Malavieille, J., Sénéchal, G., Chatton, M., Davies, T., Larroque, C., Rousset, D., Cotte, N., Romano, C., 2012. Finding the buried record of past earthquakes with GPR-based palaeoseismology: a case study on the Hope fault, New Zealand. Geophysical Journal International 189, 73–100.

Betz, D., Führer, F., Greiner, G., Plein, E., 1987. Evolution of the Lower Saxony Basin. Tectonophysics 137, 127–170.

Brandes, C., Tanner, D.C., 2012. Three-dimensional geometry and fabric of shear deformation-bands in unconsolidated Pleistocene sediments. Tectonophysics 518–521, 84–92.

Brandes, C., Polom, U., Winsemann, J., 2011. Reactivation of basement faults: interplay of ice-sheet advance, glacial lake formation and sediment loading. Basin Research 23, 53–64.

Brandes, C., Winsemann, J., 2013. Soft-sediment deformation structures in NW Germany caused by Late Pleistocene seismicity. International Journal of Earth Sciences 102, 2255–2274.

Brandes, C., Winsemann, J., Roskosch, J., Meinsen, J., Tanner, D.C., Frechen, M., Steffen, H., Wu, P., 2012. Activity of the Osning thrust in Central Europe during the Late Glacial: ice-sheet and lithosphere interactions. Quaternary Science Reviews 38, 49–62.

Brandes, C., Schmidt, C., Tanner, D.C., Winsemann, J., 2013. Paleostress pattern and salt tectonics within a developing foreland basin (northwestern Subhercynian Basin, northern Germany). International Journal of Earth Sciences 102, 2239–2254.

Bristow, C., Jol, H.M. (Eds.), 2003. Ground Penetrating Radar in Sediments. Geological Society, London, Special Publications 211 (330 pp.).

Busby, J.P., Merritt, J.W., 1999. Quaternary deformation mapping with ground penetrating radar. Journal of Applied Geophysics 41, 75–91.

Cai, J., McMechan, G.A., Fisher, M.A., 1996. Application of ground-penetrating radar to investigation of near-surface fault properties in the San Francisco Bay region. Bulletin of the Seismological Society of America 86, 1459–1470.

Carpentier, S.F.A., Green, A.G., Doetsch, J., Dorn, C., Kaiser, A.E., Campbell, F., Horstmeyer, H., Finnemore, M., 2012. Recent deformation of Quaternary sediments as inferred from GPR images and shallow P-wave velocity tomograms: Northwest Canterbury Plains, New Zealand. Journal of Applied Geophysics 81, 2–15.

Cashman, S.M., Baldwin, J.N., Cashman, K.V., Swanson, K., Crawford, R., 2007. Microstructures developed by coseismic and aseismic faulting in near-surface sediments, San Andreas fault, California. Geology 35, 611–614.

Chow, J., Angelier, J., Hua, J.-J., Lee, J.-C., Sun, R., 2001. Paleoseismic event and active faulting: from ground penetrating radar and high-resolution seismic reflection profiles across the Chihshang Fault, eastern Taiwan. Tectonophysics 333, 241–259.

Christie, M., Tsoflias, G.P., Stockli, D.F., Black, R., 2009. Assessing fault displacement and off-fault deformation in an extensional tectonic setting using 3-D ground-penetrating radar imaging. Journal of Applied Geophysics 68, 9–16.

Chwatal, W., Häusler, H., Kreutzer, I., Scheibz, J., Steirer, F., 2015. Detecting fold structures at the southern flank of the Neogene Vienna Basin in eastern Austria using near-subsurface geophysical methods. Interpretation 3, SY13–SY26.

Demanet, D., Renardy, F., Vanneste, K., Jongmans, D., Camelbeeck, T., Meghraoui, M., 2001. The use of geophysical prospecting for imaging active faults in the Roer Graben, Belgium. Geophysics 66, 78–89.

Dorn, C., Linde, N., Doetsch, J., Le Borgne, T., Bour, O., 2012. Fracture imaging within a granitic rock aquifer using multiple-offset single-hole and cross-hole GPR reflection data. Journal of Applied Geophysics 78, 123–132.

Drahor, M.G., Berge, M.A., 2017. Integrated geophysical investigations in a fault zone located on southwestern part of Izmir city, Western Anatolia, Turkey. Journal of Applied Geophysics 136, 114–133.

Du Bernard, X., Eichhubl, P., Aydin, A., 2002. Dilation bands: a new form of localized failure in granular media. Geophysical Research Letters 29 (24), 29-1–29-4.

Eichhubl, P., Hooker, J.N., Laubach, S.E., 2010. Pure and shear-enhanced compaction bands in Aztec Sandstone. Journal of Structural Geology 32, 1873–1886.

Ercoli, M., Cristina, P., Francesca, R.C., Emanuele, F., Roberto, V., 2015. Imaging of an active fault: comparison between 3D GPR data and outcrops at the Castrovillari fault, Calabria, Italy. Interpretation 3, SY57–SY66.

Forte, E., Pipan, M., Casabianca, D., Di Cuia, R., Riva, A., 2012. Imaging and characterization of a carbonate hydrocarbon reservoir analogue using GPR attributes. Journal of Applied Geophysics 81, 76–87.

Fossen, H., Hesthammer, J., 1997. Geometric analysis and scaling relations of deformation bands in porous sandstone. Journal of Structural Geology 19, 1479–1493.

Fossen, H., Johansen, T.E.S., Hesthammer, J., Rotevatn, A., 2005. Fault interaction in porous sandstone and implications for reservoir management; examples from southern Utah. American Association of Petroleum Geologists Bulletin 89, 1593–1606.

Fossen, H., Schultz, R.A., Shipton, Z.K., Mair, K., 2007. Deformation bands in sandstone: a review. Journal of the Geological Society 164, 755–769.

Gast, R., Gundlach, T., 2006. Permian strike slip and extensional tectonics in Lower Saxony, Germany. Zeitschrift der Deutschen Gesellschaft für Geowissenschaften 157, 41–55.

Grasmueck, M., Weger, R., Horstmeyer, H., 2005. Full-resolution 3D GPR imaging. Geophysics 70, K12–K19.

Green, A., Gross, R., Holliger, K., Horstmeyer, H., Baldwin, J.N., 2003. Results of 3-D georadar surveying and trenching the San Andreas fault near its northern landward limit. Tectonophysics 368, 7–23.

Grégoire, C., Halleux, L., Lukas, V., 2003. GPR abilities for the detection and characterisation of open fractures in a salt mine. Near Surface Geophysics 1, 139–147.

Grützner, C., Reicherter, K., Hübscher, C., Silva, P.G., 2012. Active faulting and neotectonics in the Baelo Claudia area, Campo de Gibraltar (southern Spain). Tectonophysics 554–557, 127–142.

Grützner, C., Fischer, P., Reicherter, K., 2016. Holocene surface ruptures of the Rurrand Fault, Germany – insights from paleoseismology, remote sensing and shallow geophysics. Geophysical Journal International 204, 1662–1677.

Hardy, S., McClay, K., 1999. Kinematic modelling of extensional fault-propagation folding. Journal of Structural Geology 21, 695–702.

Hesthammer, J., Fossen, H., 2001. Structural core analysis from the Gullfaks area, northern North Sea. Marine and Petroleum Geology 18, 411–439.

Igel, J., Günther, T., Kuntzer, M., 2013. Ground-penetrating radar insight into a coastal aquifer: the freshwater lens of Borkum Island. Hydrology and Earth System Sciences 17, 519–531.

Jin, G., Groshong, R.H., 2006. Trishear kinematic modeling of extensional fault propagation folding. Journal of Structural Geology 28, 170–183.

Kaiser, A., 2005. Neotectonic modelling of the North German Basin and adjacent areas—a tool to understand postglacial landscape evolution? Zeitschrift der Deutschen Gesellschaft für Geowissenschaften 156, 357–366.

Kettermann, M., Grützner, C., van Gent, H.W., Urai, J.L., Reicherter, K., Mertens, J., 2015. Evolution of a highly dilatant fault zone in the grabens of Canyonlands National Park, Utah, USA – integrating fieldwork, ground-penetrating radar and airborne imagery analysis. Solid Earth 6, 839–855.

Khalil, S.M., McClay, K.R., 2002. Extensional fault-related folding, northwestern Red Sea, Egypt. Journal of Structural Geology 24, 743–762.

Kley, J., Voigt, T., 2008. Late Cretaceous intraplate thrusting in central Europe: effect of Africa-Iberia-Europe convergence, not Alpine collision. Geology 36, 839–842.

Kley, J., Franzke, H.-J., Jähne, F., Krawczyk, C., Lohr, T., Reicherter, K., Scheck-Wenderoth, M., Sippel, J., Tanner, D., van Gent, H., 2008. Strain and stress. In: Littke, R., Bayer, U., Gajewski, D., Nelskamp, S. (Eds.), Dynamics of complex intracontinental basins. The Central European Basin System. Springer, Berlin, pp. 97–124.

Kockel, F., 2003. Inversion structures in Central Europe - expressions and reasons, an open discussion. Netherlands Journal of Geosciences 82, 367–382.

Lang, J., Sievers, J., Loewer, M., Igel, J., Winsemann, J., 2017. 3D architecture of cyclic-step and antidune deposits in glacigenic subaqueous fan and delta settings: integrating outcrop and ground-penetrating radar data. Sedimentary Geology 362, 83–100.

Lang, J., Lauer, T., Winsemann, J., 2018. New age constraints for the Saalian glaciation in northern central Europe: implications for the extent of ice sheets and related proglacial lake systems. Quaternary Science Reviews 180, 240–259.

Liner, C.L., Liner, J.L., 1997. Application of GPR to a site investigation involving shallow faults. The Leading Edge 16, 1649–1651.

Lohr, T., Krawczyk, C.M., Tanner, D.C., Samiee, R., Endres, H., Oncken, O., Trappe, H., Kukla, P.A., 2007. Strain partitioning due to salt: insights from interpretation of a 3D seismic data set in the NW German Basin. Basin Research 19, 579–597.

McClymont, A.F., Green, A.G., Streich, R., Horstmeyer, H., Tronicke, J., Nobes, D.C., Pettinga, J., Campbell, J., Langridge, R., 2008a. Visualization of active faults using geometric attributes of 3D GPR data: an example from the Alpine Fault Zone, New Zealand. Geophysics 73:B11–B23. https://doi.org/10.1190/1.2825408.

McClymont, A.F., Green, A.G., Villamor, P., Horstmeyer, H., Grass, C., Nobes, D.C., 2008b. Characterization of the shallow structures of active fault zones using 3-D ground-penetrating radar data. Journal of Geophysical Research 113, B10315. https://doi.org/10.1029/2007JB005402.

McClymont, A.F., Villamor, P., Green, A.G., 2009. Fault displacement accumulation and slip rate variability within the Taupo Rift (New Zealand) based on trench and 3-D ground-penetrating radar data. Tectonics 28, TC4005. https://doi.org/10.1029/2008TC002334.

Medeiros, W.E., do Nascimento, A.F., Alves da Silva, F.C., Destro, N., Demétrio, J.G.A., 2010. Evidence of hydraulic connectivity across deformation bands from field pumping tests: two examples from Tucano Basin, NE Brazil. Journal of Structural Geology 32, 1783–1791.

Meschede, M., Asprion, U., Reicherter, K., 1997. Visualization of tectonic structures in shallow-depth high-resolution ground-penetrating radar (GPR) profiles. Terra Nova 9, 167–170.

Mollema, P.N., Antonellini, M.A., 1996. Compaction bands: a structural analog for anti-mode I cracks in aeolian sandstone. Tectonophysics 267, 209–228.

Neal, A., 2004. Ground-penetrating radar and its use in sedimentology: principles, problems and progress. Earth-Science Reviews 66, 261–330.

Pettijohn, F.J., Potter, P.E., Siever, R., 1973. Sand and sandstone. Springer Verlag, Berlin, p. 617.

Qu, D., Tveranger, J., 2016. Incorporation of deformation band fault damage zones in reservoir models. American Association of Petroleum Geologists Bulletin 100, 423–443.

Reicherter, K., Kaiser, A., Stackebrandt, W., 2005. The post-glacial landscape evolution of the North German Basin: morphology, neotectonics and crustal deformation. International Journal of Earth Sciences 94, 1083–1093.

Reiss, S., Reicherter, K.R., Reuther, C.-D., 2003. Visualization and characterization of active faults and associated sediments by high-resolution GPR. In: Bristow, C.S., Jol, H.M. (Eds.), Ground Penetrating Radar in Sediments. Geological Society, London, Special Publication vol. 211, pp. 247–255.

Roskosch, J., Winsemann, J., Polom, U., Brandes, C., Tsukamoto, S., Weitkamp, A., Bartholomäus, W.A., Henningsen, D., Frechen, M., 2015. Luminescence dating of ice-marginal deposits in northern Germany: evidence for repeated glaciations during the Middle Pleistocene (MIS 12 to MIS 6). Boreas 44, 103–126.

Salvi, S., Cinti, F.R., Colini, L., D'Addezio, G., Doumaz, F., Pettinelli, E., 2003. Investigation of the active Celano-L'Aquila fault system, Abruzzi (central Apennines, Italy) with combined ground-penetrating radar and palaeoseismic trenching. Geophysical Journal International 155, 805–818.

Sharp, I.R., Gawthorpe, R.L., Underhill, J.R., Gupta, S., 2000. Fault-propagation folding in extensional settings: examples of structural style and synrift sedimentary response from the Suez rift, Sinai, Egypt. Geological Society of America Bulletin 112, 1877–1899.

Shipton, Z.K., Cowie, P.A., 2001. Damage zone and slip-surface evolution over μm to km scales in high-porosity Navajo sandstone, Utah. Journal of Structural Geology 23, 1825–1844.

Shipton, Z.K., Evans, J.P., Thompson, L.B., 2005. The geometry and thickness of deformation band fault core and its influence on sealing characteristics of deformation-band fault zones. In: Sorkhabi, R., Tsuji, Y. (Eds.), Faults, Fluid Flow, and Petroleum Traps. American Association of Petroleum Geologists Memoir vol. 85, pp. 181–195.

Shipton, Z.K., Meghraoui, M., Monro, L., 2017. Seismic slip on the west flank of the Upper Rhine Graben (France-Germany): evidence from tectonic morphology and cataclastic deformation bands. In: Landgraf, A., Kuebler, S., Hintersberger, E., Stein, S. (Eds.), Seismicity, Fault Rupture and Earthquake Hazards in Slowly Deforming Regions. Geological Society, London, Special Publication 432, pp. 147–161.

Soliva, R., Ballas, G., Fossen, H., Philit, S., 2016. Tectonic regime controls clustering of deformation bands in porous sandstone. Geology 44, 423–426.

Stevens, K.M., Lodha, G.S., Holloway, A.L., Soonawala, N.M., 1995. The application of ground penetrating radar for mapping fractures in plutonic rocks within the Whiteshell Research Area, Pinawa, Manitoba, Canada. Journal of Applied Geophysics 33, 125–141.

Tanner, D.C., Krawczyk, C.M., 2017. Restoration of the Cretaceous uplift of the Harz Mountains, North Germany: evidence for the geometry of a thick-skinned thrust. International Journal of Earth Sciences 106, 2963–2972.

Theune, U., Rokosh, D., Sacchi, M.D., Schmitt, D.R., 2006. Mapping fractures with GPR: A case study from Turtle Mountain. Geophysics 71, B139–B150.

Tindall, S.E., 2014. Simple calculations of fluid flow across jointed cataclastic deformation bands. Marine and Petroleum Geology 57, 152–159.

Torabi, A., Fossen, H., 2009. Spatial variation of microstructure and petrophysical properties along deformation bands in reservoir sandstones. American Association of Petroleum Geologists Bulletin 93, 919–938.

Tronicke, J., Villamor, P., Green, A.G., 2006. Detailed shallow geometry and vertical displacement estimates of the Maleme Fault Zone, New Zealand, using 2D and 3D georadar. Near Surface Geophysics 4, 155–161.

Van Dam, R., 2012. Landform characterization using geophysics—recent advances, applications, and emerging tools. Geomorphology 137, 57–73.

Van Dam, R., Schlager, W., 2000. Identifying causes of ground-penetrating radar reflections using time-domain reflectometry and sedimentological analyses. Sedimentology 47, 435–449.

van Wees, J.D., Stephenson, R.A., Ziegler, P.A., Bayer, U., McCann, T., Dadlez, R., Gaupp, R., Narkiewicz, M., Bitzer, F., Scheck, M., 2000. On the origin of the southern Permian basin, Central Europe. Marine and Petroleum Geology 17, 43–59.

Winsemann, J., Asprion, A., Meyer, T., Schramm, C., 2007. Facies characteristics of Middle Pleistocene (Saalian) ice-margin subaqueous fan and delta deposits, glacial Lake Leine, NW Germany. Sedimentary Geology 193, 105–129.

Zuluaga, L.F., Rotevatn, A., Keilegavlen, E., Fossen, H., 2016. The effect of deformation bands on simulated fluid flow within fault-propagation fold trap types: lessons from the San Rafael monocline, Utah. American Association of Petroleum Geologists Bulletin 100, 1523–1540.